



High-ionic-strength electroosmotic flows in uncharged hydrophobic nanochannels

Daejoong Kim^{a,*}, Eric Darve^b

^a Department of Mechanical Engineering, Sogang University, Seoul, Republic of Korea

^b Department of Mechanical Engineering, Stanford University, Stanford, CA 94305, USA

ARTICLE INFO

Article history:

Received 15 July 2008

Accepted 10 October 2008

Available online 12 November 2008

Keywords:

Electroosmosis

High ionic strength

Zero surface charge

Molecular dynamics simulation

ABSTRACT

We report molecular dynamics simulation results of high-ionic-strength electroosmotic flows inside uncharged nanochannels. The possibility of this unusual electrokinetic phenomenon has been discussed by Dukhin et al. [A. Dukhin, S. Dukhin, P. Goetz, *Langmuir* 21 (2005) 9990]. Our computed velocity profiles clearly indicate the presence of a net flow with a maximum velocity around 2 m/s. We found the apparent zeta potential to be -29.7 ± 6.8 mV, using the Helmholtz–Smoluchowski relation and the measured mean velocity. This value is comparable to experimentally measured values in Dukhin et al. and references therein. We also investigate the orientations of water molecules in response to an electric field by computing polarization density. Water molecules in the bulk region are oriented along the direction of the external electric field, while their near-wall orientation shows oscillations. The computation of three-dimensional density distributions of sodium and chloride ions around each individual water molecule show that chloride ions tend to concentrate near a water molecule, whereas sodium ions are diffusely distributed.

© 2008 Elsevier Inc. All rights reserved.

1. Introduction

The classical Gouy–Chapman–Stern (GCS) model [1] has been successfully applied for theoretical and experimental treatments in electrokinetics. In the light of the GCS model, a so-called electrical double layer (EDL), which consists of a diffuse layer and a stagnant Stern layer, is an equilibrium structure with the balance of thermal energy of ions and electrostatic energy between surface charges and ions. Despite its successful application to low and intermediate ionic strength electrolytes, the GCS model fails to explain electrokinetic phenomena for high-ionic-strength electrolytes [2]. The model indeed predicts that increasing ionic strength should collapse the EDL and thus suppress electrokinetic phenomena. Recent experimental works, however, have shown the existence of such phenomena.

Deinega et al. [3] first reported electrokinetic phenomena for high-ionic-strength electrolytes in 1982, according to Dukhin et al. [4]. Many groups have reported convincing experimental evidence since then. Recent experimental results are especially indebted to the advancement of an electroacoustic technique in the 1990s [5]. This technique makes possible reliable measurements of electrokinetic phenomena for high-ionic-strength electrolytes by avoiding issues related to traditional methods, such as unstable dispersions, Joule heating, etc. [2]. Johnson et al. reported mea-

sured ζ potentials as high as 30 mV with α -alumina and various solutions of 1 M salt concentration [6]. Kosmulski and Rosenholm reviewed experimental results for various solid surfaces and solutions and all these results confirm the existence of electrokinetic phenomena for high-ionic-strength electrolytes and sometimes demonstrate decently high ζ potential, as in Johnson et al.'s results [2].

Dukhin et al. recently reported results consistent with Johnson et al.'s, using the electroacoustic technique [4]. Noting that there was no theoretical description in previous studies, they explained these experimental results by their “zero-surface-charge” double-layer hypothesis. Its key concept is the separation of finite electric charges within the surface water layer, which leads to the formation of a different type of double layer. This may be possible because cations and anions have different abilities to penetrate into the surface water layer. Another interesting point of this paper is finite zeta potentials for a surface with nonionic surfactants (Tween 80), which supposedly has no surface charge. They explained this unusual electrokinetic phenomenon (i.e., no surface charge and high-ionic-strength) using their hypothesis. In this paper, we study the same electrokinetic situation inside nanochannels using molecular dynamics (MD) and investigate Dukhin et al.'s hypothesis.

MD simulation has been successfully performed to study microscopic or molecular structures of EDLs and electrokinetic phenomena (for example, Lyklema et al. [7]). It is useful to find, for example, the distribution of ion density in EDLs, which is difficult to measure experimentally. We briefly review recent studies

* Corresponding author.

E-mail address: daejoong@sogang.ac.kr (D. Kim).

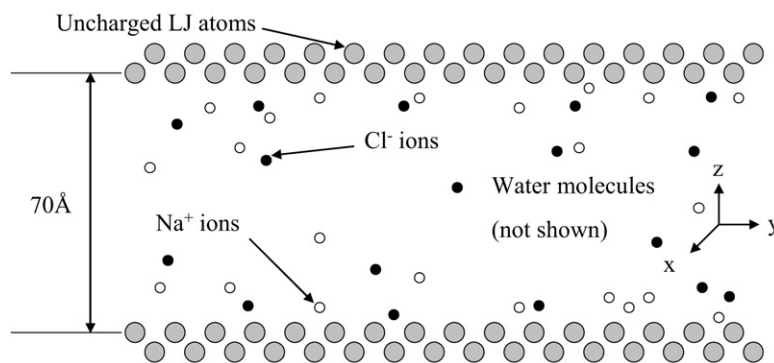


Fig. 1. Model system in this paper. It includes two uncharged flat plates, 32 cations, 32 anions, and 3396 water molecules. We applied a periodic boundary conditions with each unit cell having a $30 \text{ \AA} \times 48 \text{ \AA} \times 70 \text{ \AA}$ channel. We inserted a vacuum space of 400 \AA between two periodic images along the z direction, to mimic a pseudo-two-dimensional system. The coordinate system is also shown.

of MD simulation of electrokinetic phenomena in nanochannels. Freund [8], Zhu et al. [9], and Qiao and Aluru [10] compared continuum-based Poisson–Boltzmann theory and their MD results. A major difference is different ion distributions, especially near solid surfaces, partly due to layering of water molecules. Zhu et al. and Qiao and Aluru proposed ways to compensate this discrepancy and showed improved agreements. Qiao and Aluru published a number of papers on interesting electrokinetic phenomena, using MD as their main tool [11–13]. Joseph and Aluru recently performed a multiscale simulation to show detailed water and ion transport properties [14]. Joly and co-workers showed that hydrophobicity of solid surfaces amplifies the ζ potential by stimulating streaming currents [15]. In their subsequent papers, Joly and co-workers confirmed their previous study, finding consistent results in diverse electrokinetic situations [16,17]. Kim and Darve [18] studied the effects of surface roughness and did a comparison of their MD results with the Poisson–Boltzmann theory. They showed that the flow rate and ζ potential decrease with increasing roughness.

All the computational models above correspond to high-ionic-strength electrokinetics, although this point was not explicitly noted. The reason for this high-ionic-strength is limited computational resources (a large number of ions are required to obtain enough statistics). In most previous works, solid surfaces are charged as in usual electrokinetic systems. We here explore high-ionic-strength electrokinetics in uncharged nanochannels. In the main body of this paper, we start with computed profiles for density of water molecules and ions, charge density, electric potential, and electroosmotic velocity. We then discuss the ζ potential for this unusual electrokinetic system in nanochannels. In order to understand the behavior of water molecules and ions in more detail, we computed water orientation through polarization density and we also computed the three-dimensional distribution of ions around an individual water molecule.

2. Physical models and computational methods

Fig. 1 shows the model system of this paper, with the definition of the coordinate system. The origin lies at the midplane of the channel (i.e., $z = 0$). We plot a parameter of interest, e.g., density, in the x axis and the z coordinate in the y axis in many figures of this paper, as we are interested in its z -directional variation.

The walls have hexagonal close-packed (HCP) structures with a lattice constant $a = \sigma_{\text{Wall-Wall}} = 3 \text{ \AA}$ ($\sigma_{\text{Wall-Wall}}$ is the Lennard–Jones length scale between two wall atoms in Table 1). We treat each wall atom as a Lennard–Jones atom fixed at a lattice site. Upper and lower walls have two layers of wall atoms each and the two adjacent layers are separated by $1.25\sigma_{\text{Wall-Wall}}$. We applied periodic boundary conditions for all three dimensions, and the

Table 1
Lennard–Jones parameters.

Atom type	σ (nm)	ϵ (kJ/mol)
O–O	0.31	0.72
Na ⁺ –O	0.28	0.20
Na ⁺ –Na ⁺	0.26	0.062
Cl [–] –O	0.38	0.54
Cl [–] –Na ⁺	0.34	0.16
Cl [–] –Cl [–]	0.44	0.44
Wall–O	0.31	1.1
Wall–Na ⁺	0.28	0.34
Wall–Cl [–]	0.37	0.92
Wall–wall	0.30	1.9

Note. We used the GROMOS-96 forcefield except for wall atoms, whose parameters are from Zhou et al. [21]. Between wall atoms and the other types of atom, we applied the Lorentz–Berthelot combination rule.

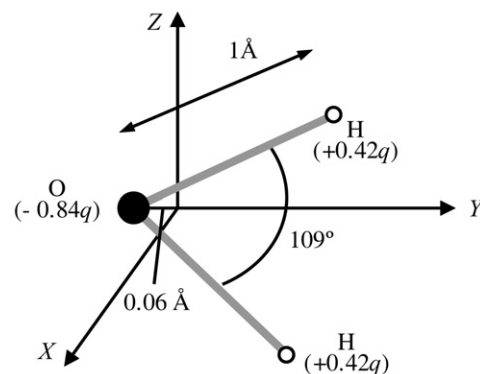


Fig. 2. Extended simple point charge model (SPC/E) applied for water molecules. We defined a water-centered coordinate system (with the origin at the center of mass of a water molecule). The direction of a water dipole moment is the same as the Y axis.

channel dimension in each unit cell is $30 \times 48 \times 70 \text{ \AA}$ ($x \times y \times z$). We placed a vacuum space of 400 \AA between the two periodic images along the z direction to achieve a pseudo-two-dimensional system in the yz plane (we applied the electric field along the y direction). Overall, the model system can be assumed to be an electrolytic solution enclosed by two infinite parallel flat plates with zero charge.

The model electrolytic solution includes 32 cations, 32 anions, and 3396 water molecules. The bulk concentration of the electrolyte is 0.53 M , based on the channel size and the number of ions. We modeled ions as point charges with the Lennard–Jones potentials. For water molecules (Fig. 2), we used the extended simple point charge model (SPC/E) [19]. We will present the ion density distribution around each water molecule. For that, we define a water-centered coordinate system, shown in Fig. 2. The origin of

this coordinate system is located at the center of mass of a water molecule, which is indeed in close proximity to the oxygen atom location. The XY plane is the plane containing an oxygen atom and two hydrogen atoms. Note also that the direction of a water dipole moment coincides with the Y axis.

We used the GROMACS code [20] with the GROMOS-96 force-field except for wall atoms. The forcefield includes the 12–6 Lennard–Jones and electrostatic potentials and thus the potential energy between two atoms i and j , separated by r , can be expressed as

$$V_{ij}(r) = 4\epsilon \left\{ \left(\frac{\sigma}{r} \right)^{12} - \left(\frac{\sigma}{r} \right)^6 \right\} + \epsilon \frac{q_i q_j}{r}. \quad (1)$$

The walls are chosen to be similar to silica. The Lennard–Jones parameters are identical to the parameters for silica wall atoms in Zhou et al. [21], but we did not attempt to accurately model real silica walls with their specific morphologies. We applied the Lorentz–Berthelot combination rule for the Lennard–Jones interactions of wall atoms with other types of atoms, which are not included in the GROMOS-96 forcefield. All the Lennard–Jones parameters are summarized in Table 1. The cutoff radius for the Lennard–Jones potential was 7 Å. For the calculation of electrostatic potentials, we adopted the particle-mesh Ewald (PME) method [22]. To constrain water molecules, we used the SETTLE algorithm, which is an analytical solution of the SHAKE algorithm specific for water [23]. For time integration, we applied the Berendsen thermostat [24] combined with the velocity Verlet integration algorithm with a time step of 1 fs. The time constant for the thermostat was 0.1 ps with a reference temperature of 300 K.

We generated an initial configuration by randomly distributing cations and anions in water slabs inside a nanochannel. We then performed energy minimization (the steepest descent algorithm) to avoid undesired van der Waals contacts. Before starting MD simulation, we assigned random numbers to initial velocities of water molecules and ions, according to the Maxwell distribution at 300 K. We performed 0.5-ns-long (equilibrium) MD simulation without an electric field and subsequently 0.5-ns-long (nonequilibrium) MD simulation with an electric field, both as equilibration steps. Production runs lasted for 12 ns in total with a sampling rate of 50 fs, using the following procedure. (1) We did the first production run for 1 ns. (2) During this first run, we sampled a configuration and took it as an initial configuration for a subsequent production run. (3) We reassigned initial velocities, with a different seed for the random number generator. (4) We performed the same equilibration step, i.e., a 0.5-ns-long run without an electric field and a 0.5-ns-long run with an electric field. (5) We performed another 1-ns-long production run. We repeated (actually, in parallel) this procedure 11 times and thus the total duration of production runs was 12 ns. By doing this procedure, we expect to exclude any possibility of a biasing effects of initial velocities on the final results and also to decrease computation time. The electric field strength applied in the y direction was 0.1 V/nm. The reason for this strong electric field is to increase the signal-to-noise ratio, i.e., to obtain a “measurable” mean flow field compared to the thermal noise, which is problematic otherwise even after the complex procedure described above. With small electric fields, the convergence of the statistics should be very slow and lead to unacceptable computational time. The magnitude of an electric field in this work is of the same order as in previous works [8,10,11,18].

3. Results and discussions

3.1. Density profiles of water molecules and ions

Fig. 3 shows the density profiles of water and ions and a charge density distribution. The dotted lines indicate the error bounds

with 95% confidence. In Fig. 3a for the water density profile, the dotted lines are overlapped with the solid line, since the sampling errors are negligible. From the figure, we can find layering of water molecules, indicated by the oscillating density profile near the wall. This phenomenon has been studied experimentally as well as computationally and it is well explained elsewhere, for example, in Israelachvili [25]. We observed three distinct layers, whereas up to five layers have been reported previously [26].

The overall density profiles for both ions (Figs. 3c and 3d) show peaks between $z = -25$ Å and $z = -30$ Å and decrease rapidly toward the wall and slowly away from the wall. The presence of peaks is somewhat counterintuitive, as one would expect rather uniform density inside the nanochannel enclosed by uncharged surfaces. A similar increased concentration of ions near a gas/liquid interface has been recently reported by Mucha et al. [27]. They found consistent results for ion density profiles in acid, base, and salt solutions, including HCl, HBr, HI, NaOH, NaCl, and NaI, from their combined experimental and computational studies (MD simulation used as their computation tool). This near-wall profile can be explained by the specific adsorption and hydration force of ions [4,27]. We found that the decrease of ion densities toward and away from the wall is not monotonic but oscillatory (with some noise). These oscillatory shapes are attributed to volume exclusion due to water layering [10].

Another interesting point in the ion density profiles is different first peak locations of two ions near the wall. We initially expected the sodium ion peak to be closer to the wall than the chloride ion peak, based on their size ($\sigma_{\text{Cl}^- - \text{Wall}} = 3.7$ Å $>$ $\sigma_{\text{Na}^+ - \text{Wall}} = 2.8$ Å). The computed density profiles, however, show the opposite. Mucha et al. also found the same trend, i.e., positive ion repulsion from a gas/liquid interface [27]. They observed that positive ions in bases and salt solutions are repelled from the wall. This indicates that the ion-specific propensities as well as the ion size determine the distributions of ions [27].

The consequence of the near-wall increased concentrations and different peak locations for sodium and chloride ions is a nonzero charge density distribution inside the nanochannel, shown in Fig. 3b. The charge density is significant, especially near the wall, whereas it looks like a noise or a sampling error in the bulk region (say, $|z| < 25$ Å). The positive peak is at $z = -27$ Å and the negative one is at $z = -29$ Å. If a charge density distribution were computed for salt solutions in Mucha et al.’s work [27], it would be similar to Fig. 3b, with a negative peak near the wall and a positive peak away from it.

3.2. Electroosmotic flows and the ζ potential

Fig. 4a shows the velocity profile of an electroosmotic flow inside the uncharged nanochannel. The error bounds (95% confidence) are indicated by the dotted lines. It clearly indicates the presence of a net flow with a maximum velocity around 2 m/s, albeit with some noise due to thermal fluctuations. From the velocity profile, we can also estimate the shear plane to be around $z = -32$ Å; this corresponds to the first peak in the water density profile. The overall velocity profile suggests that the wall is hydrophobic. Joly et al. recently reported the amplification of electroosmotic flows on charged surfaces due to hydrophobicity [15,16]. We address below a similar amplification of flows on uncharged surfaces.

The ζ potential is usually considered to be the critical parameter for electroosmotic flows. Its proper definition, however, is unclear for our case with uncharged surfaces. We here define the ζ potential using the Helmholtz–Smoluchowski relation (see below). This ζ potential is the apparent potential that would be measured in an experiment like in Dukhin et al. [4]. We will see that this potential is different from the electric potential measured

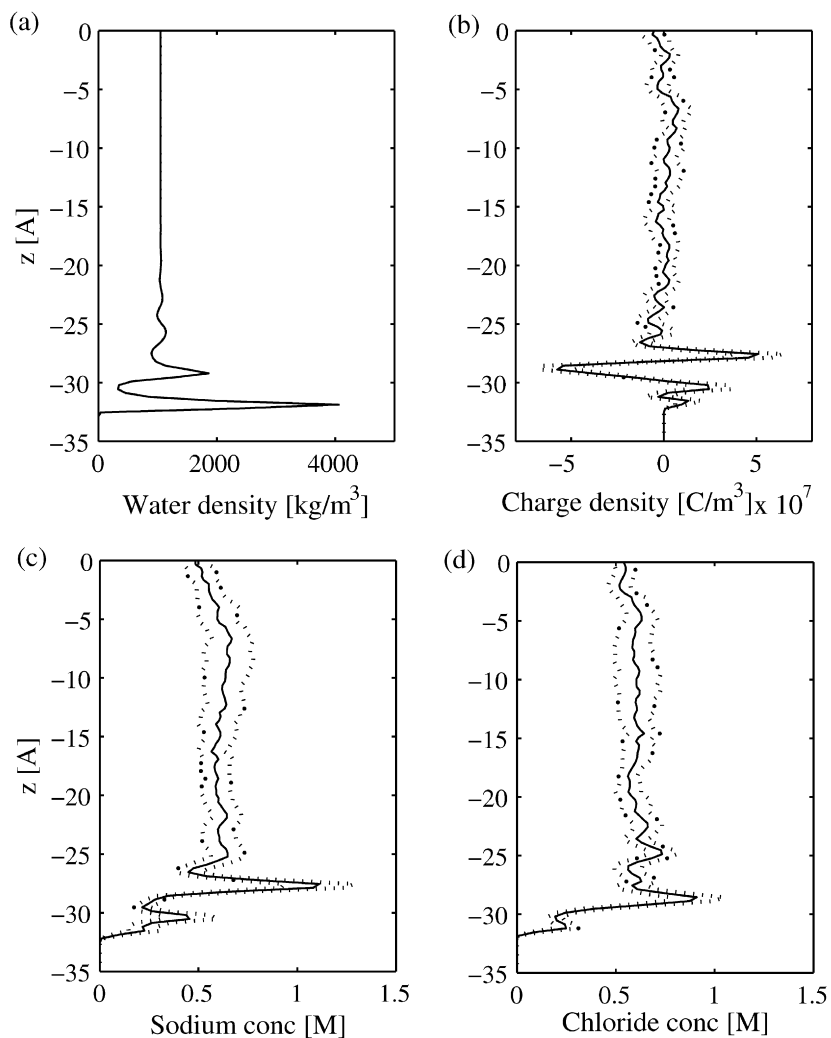


Fig. 3. One-dimensional profiles for (a) water density, (b) charge density, and molar concentration of (c) sodium and (d) chloride ions. The error bounds (95% confidence) are indicated by the dotted lines.

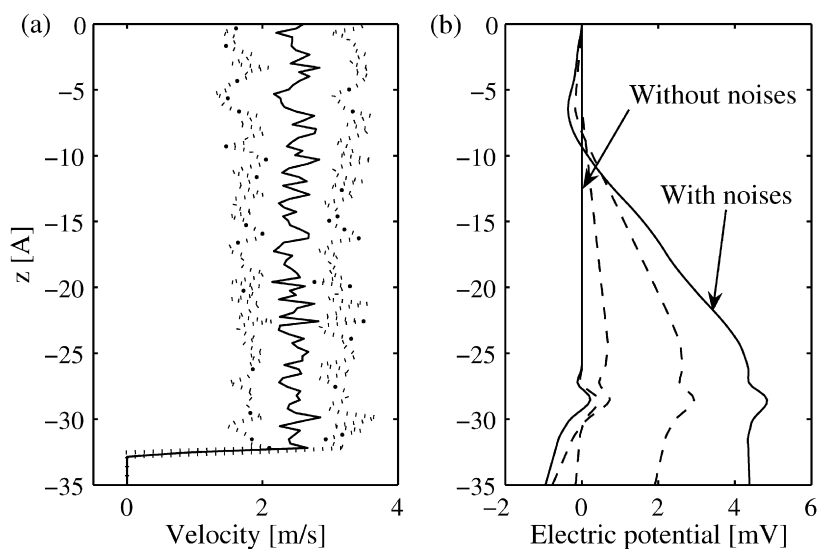


Fig. 4. One-dimensional profile for (a) electroosmotic flow velocity inside the uncharged nanochannel and (b) electric potential. The dotted lines in the velocity profile indicate error bounds with a 95% confidence. Different lines in the electric potential profile are from several calculation methods.

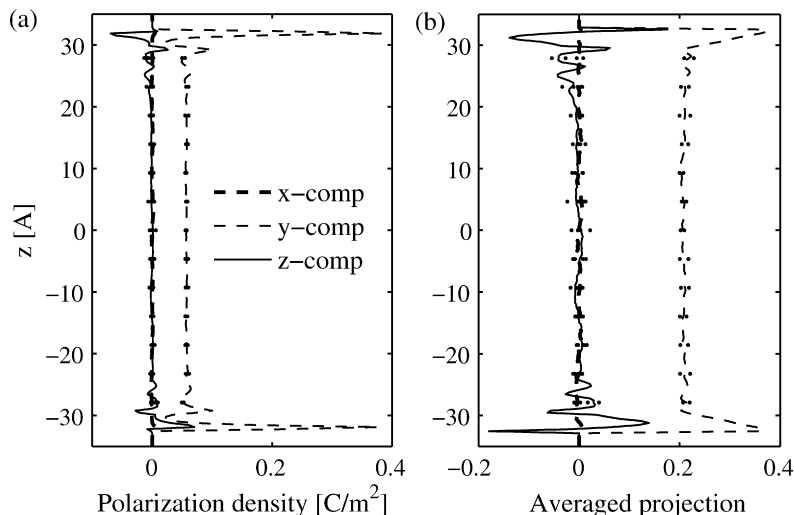


Fig. 5. (a) Polarization density and (b) averaged projection of water molecules with error bounds. While polarization density depends on water density, averaged projection is a good measure for the preferred orientation of water molecules.

at the shear plane, which should be the same in the Debye–Huckel limit [1] or at least similar in the case of typical charged surfaces.

To use the Helmholtz–Smoluchowski relation, we first calculate the volume-averaged velocity, using

$$u_{\text{EOF}} \equiv \frac{1}{V} \int_V v(x, y, z) dx dy dz, \quad (2)$$

where v is the velocity at the location (x, y, z) and V is the channel volume. The Helmholtz–Smoluchowski relation is given as

$$u_{\text{EOF}} = -\frac{\epsilon E \zeta}{\mu}, \quad (3)$$

where ϵ is the permittivity ($\epsilon = \epsilon_0 \epsilon_r$ and $\epsilon_r = 77.8$ for water at 300 K) and μ is the viscosity. From these equations, we estimated the ζ potential to be -29.7 ± 6.8 mV. This is comparable to the value found experimentally in Dukhin et al. and references therein [4].

To compute the electric potential at the shear plane (another possible ζ potential definition), we first calculate the electrical potential profile from the charge density distribution in Fig. 3b. We can obtain the electrical potential by integrating the Poisson equation, $\epsilon \nabla^2 \phi = -\rho_E$ (ϕ is the electrical potential, ϵ is the permittivity of water, and ρ_E is the charge density), with the reference at the midplane ($\phi = 0$). We found, however, that it is not as straightforward as it first sounds, since this electric potential computation is greatly affected by charge density noise in the bulk region ($|z| < 25$ Å). The computation with the noise included shows that the potential at the shear plane ($z = -32$ Å) is 4.2 mV. However, if we completely remove the noise in $|z| < 25$ Å, i.e., assume a single averaged value in the bulk, this value becomes -0.8 mV. We computed electrical potentials with different noise reduction methods and show these values with the dashed lines in the figure. Overall, the electrical potential at the shear plane is well within ± 5 mV, which is significantly different from the apparent ζ potential using the Helmholtz–Smoluchowski relation.

The discrepancy between the two potentials is now in question. One study to be noted here is Joseph and Aluru’s multiscale simulation for uncharged silica slits and 1 M KCl solutions [14]. They obtained an apparent ζ potential of -8 mV on a hydrophilic surface. This value is rather close to the electrical potential at the shear plane in our simulation (Joseph and Aluru did not calculate electrical potentials). We think that this discrepancy could be

explained with Joly et al.’s hydrophobic amplification argument, written as

$$\zeta = V_0 \left(1 + \frac{b}{\lambda} \right), \quad (4)$$

where ζ is the amplified potential, V_0 is the potential inherent in the surface (bare potential), λ is the Debye length, and b is the slip length [28]. This equation tells us that the greater the slip length, the greater the difference between the amplified potential and the bare potential. In Joseph and Aluru, the bare potential determined by the surface (and possibly a nonzero charge density distribution) would coincide with the apparent potential with their hydrophilic surface ($b = 0$). In our case, however, the apparent ζ potential would be amplified due to the hydrophobic surface. We believe that this argument needs further study as the hydrophobicity amplification argument itself does.

3.3. Polarization density and orientation of water molecules

We computed polarization density to find the changes in the structure of water molecules in response to an electric field. Fig. 5a shows the polarization density profile of water molecules inside the uncharged nanochannel. We showed the error bounds (95% confidence), indicated by the dots, only at 13 data points to avoid too crowded lines. We define the polarization density of water molecules at a location \mathbf{r} as

$$\mathbf{P}(\mathbf{r}) \equiv \sum_n \boldsymbol{\mu}_n \delta(\mathbf{r} - \mathbf{r}_n), \quad (5)$$

where $\boldsymbol{\mu}_n$ is the dipole moment vector of a water molecule n , δ is the Kronecker delta function, and its magnitude is 2.35 D for the SPC/E water model [29]. The summation should be done for all water molecules. In practice we binned the computational domain into xy plane slabs along the z direction. In a bin i , the j -component of polarization density can be expressed as

$$P_j(z_i) = \frac{1}{V_i} \sum_{n_i} \mu \cos \theta_j^{n_i}, \quad (6)$$

where z_i is the z coordinate of the midplane of the bin i , V_i is its volume, μ is the magnitude of a water dipole moment, and $\cos \theta_j^{n_i}$ is the projection of a dipole moment of a water n_i onto the j -coordinate.

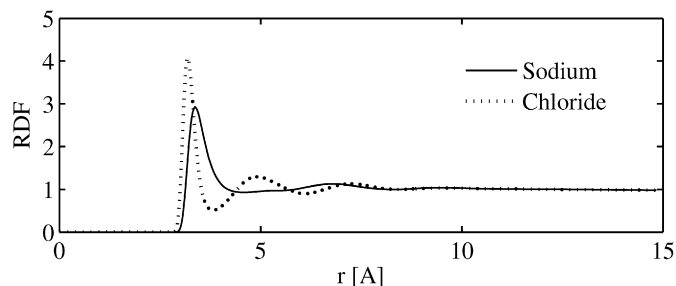


Fig. 6. Radial distribution functions of sodium and chloride ions with the center of mass of a water molecule.

This polarization density is zero when water molecules are isotropically oriented. However, walls and an electric field can constrain the motions of water molecules and thus create a nonzero component in a certain direction. Fig. 5a shows that the y and z components of polarization density have nonzero values, whereas its x component is nearly zero everywhere. The y component especially has nonzero values in the bulk region. These nonzero values here are due to the preferred orientation of water molecules in response to an electric field applied along this direction [18]. The y and z components have nonzero oscillatory profiles near the wall. This is due to the preferred orientation of water molecules related to layering phenomena. Layering of water can be explained by “solvation forces” or “hydration forces” (for water), which is again well described in Israelachvili [25].

Polarization density (albeit its physical signification) is not a direct measure of the orientation of water molecules, since it also depends on the nonuniform density of water (see Fig. 3a). We therefore normalize the polarization density by the number density and obtain the averaged projection, using

$$\langle \cos \theta_j^{n_i} \rangle \equiv \frac{\langle P_j(z_i) \rangle}{c_i \mu} \quad (7)$$

$\langle \cos \theta_j^{n_i} \rangle$ is the averaged cosine of the water dipole angle with respect to each coordinate, or the averaged projection onto each coordinate. This parameter ranges from -1 to 1 and is zero when water dipoles are isotropically oriented. It is a direct quantitative measure of the preferred orientation of water molecules. Its y component peaks are less pronounced than in the polarization density profile. The number of local maxima in the profile is also different. Fig. 5b more clearly shows that the z component has drastic oscillations, switching between positive and negative values. It is explained by layering of water molecules near the wall.

3.4. Radial distribution functions and ion density distributions

In order to investigate the interactions of ions and water molecules in more detail, we computed the radial distribution functions (RDF), shown in Fig. 6. RDF of a species B around a species A is defined as [30]

$$g_{AB}(r) \equiv \frac{\langle \rho_B(r) \rangle}{\langle \rho_B \rangle_{\text{local}}} = \frac{1}{\langle \rho_B \rangle_{\text{local}}} \frac{1}{N_A} \sum_{i \in A} \sum_{j \in B} \frac{\delta(r_{ij} - r)}{4\pi r^2}, \quad (8)$$

where $\langle \rho_B(r) \rangle$ is the density of a species B at a distance r from species A , and $\langle \rho_B \rangle_{\text{local}}$ is the average density of a species B away from a species A . In this paper, we define $\langle \rho_B \rangle_{\text{local}}$ as the averaged density of a species B 10 Å apart from a species A . The RDF of a sodium ion and a chloride ion with respect to the center of mass of a water molecule show some differences (see Fig. 6). The RDF of a sodium ion has one pronounced peak, whereas that of a chloride ion has two pronounced peaks. The first peak itself is greater for a chloride ion than for a sodium ion. The RDF of a sodium ion

is almost constant at $r > 4$ Å but that of a chloride ion becomes constant farther apart from the water molecule. Overall, the distribution of sodium ions is less influenced by the presence of nearby water molecules.

The RDF of an ion can be indicative of hydration shells around the ion. In this respect, the first valley from an ion can be thought of as the size of the primary hydration shell around the ion [25]. The size of this shell for a sodium ion is larger than that of a chloride ion in Fig. 6. This result is consistent with our initial observation, i.e., the closer location of the sodium ion peak in Figs. 3c and 3d. The RDF also shows the presence of the second and third shells for a chloride ion. This indicates that water molecules are more restricted around a chloride ion than around a sodium ion. The oscillatory nature of this profile reflects the interplay between hydration forces and volume exclusion [25].

To further understand these different interactions, we computed three-dimensional density distributions of sodium and chloride ions around an individual water molecule, shown in Fig. 7. For these, we used the coordinate system shown in Fig. 2, with the center of mass of each water molecule located at the origin. We sliced the computational domain into slabs with a thickness of 4.25 Å along the Z direction. We then computed and plotted density distributions of ions in the XY plane for each slab. The slabs span $|Z| < 2.125$ Å, 2.125 Å $< |Z| < 6.375$ Å, and 6.375 Å $< |Z| < 10.625$ Å for (a)–(b), (c)–(d), and (e)–(f), respectively.

The plots for sodium and chloride ions clearly show different trends. Sodium ions are diffusely located near the oxygen atom in a water molecule, whereas chloride ions are concentrated near either of the two hydrogen atoms. This explains why the peak height for sodium ions is lower than that for chloride ions in Fig. 6. These different trends can be explained by the interplay between the Lennard–Jones and electrostatic interactions. Chloride ions are concentrated close to the hydrogen atoms because the attractive electrostatic forces between these two are much stronger than the separating forces (the near-field contribution of the Lennard–Jones interaction). In contrast, the attractive electrostatic interaction for the sodium ion–oxygen pairs is balanced with the repulsive Lennard–Jones interaction. As a result, sodium ions show diffuse distributions away from the oxygen atom.

4. Summary

Using molecular dynamics simulation, we observed high-ionic-strength electroosmotic flows inside uncharged nanochannels. This work is the first atomistic simulation of this type of flow and would serve as a discussion of Dukhin et al.’s hypothesis about its physical mechanism [4]. We found that the apparent ζ potential is as high as -29.7 ± 6.8 mV for 0.53 M sodium chloride solutions from the Helmholtz–Smoluchowski relation and the mean velocity. The nonzero charge distribution due to different locations of positive and negative ions (explained with specific adsorption and hydration forces by Mucha et al. [27]) creates nonzero electric potentials. This bare potential is found to be within ± 5 mV at the shear plane. The apparent and bare potentials should be the same in the Debye–Hückel limit but are found to be significantly different in our simulation. We believe that the significant apparent ζ potential is due to the hydrophobicity amplification explained by Joly et al. [15,16].

We also observed that water molecules show a tendency to orient themselves along a certain direction, depending on electric fields and the distance from the wall. Water molecules in the bulk region are oriented in the direction of an applied electric field. Their orientations near the wall show oscillations, which is caused by the layering of water molecules. Three-dimensional ion density distributions around each water molecule show that chloride ions are concentrated closer to a water molecule than sodium ions. This

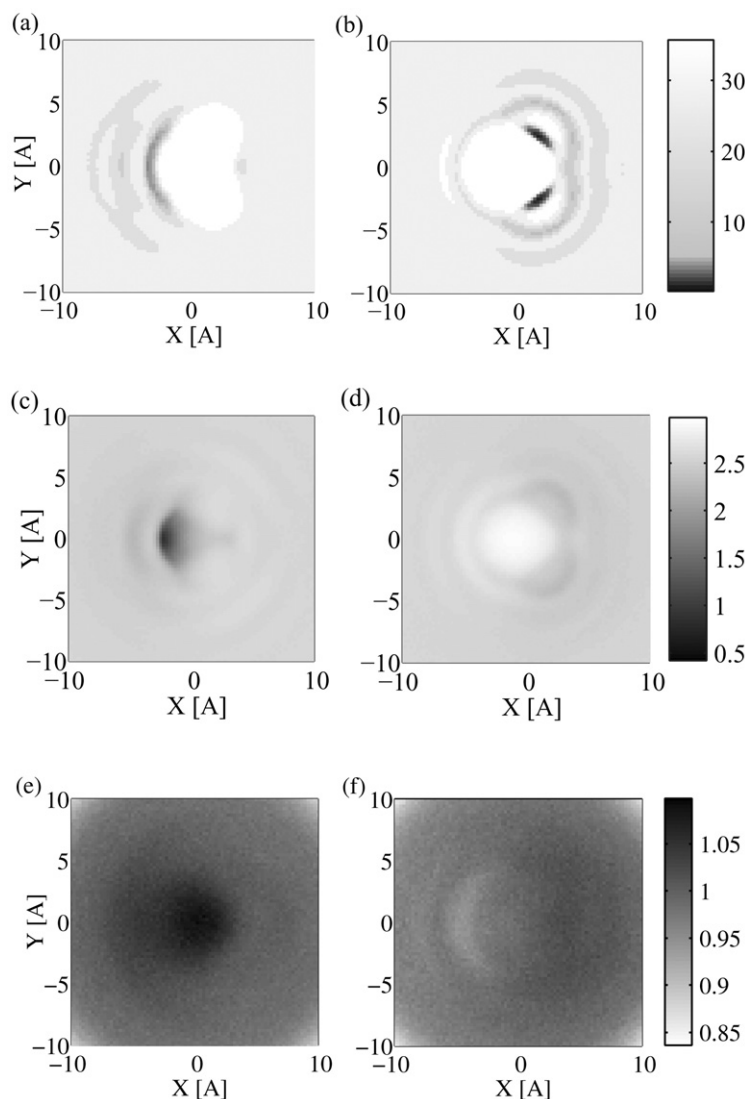


Fig. 7. Normalized density distribution of anions (left-hand column) and cations (right-hand column). (a)–(b) $|Z| < 2.125 \text{ \AA}$. (c)–(d) $2.125 \text{ \AA} < |Z| < 6.375 \text{ \AA}$. (e)–(f) $6.375 \text{ \AA} < |Z| < 10.625 \text{ \AA}$.

can be explained by the different interactions of the Lennard–Jones and electrostatic potentials between ions and water.

Acknowledgments

This work was supported by a Joint Research Initiative grant from the NASA Ames Research Center and by Sogang University Research Grant 200810026. D.K. also acknowledges supports from the Korea Research Foundation Grant by the Korean Government (KRF-2008-331-D00075) for the preparation of this manuscript.

References

- [1] J. Lyklema, *Solid–Liquid Interfaces, Fundamentals of Interface and Colloid Science*, vol. 2, Academic Press, London, 1995.
- [2] M. Kosmulski, J.B. Rosenholm, *Adv. Colloid Interface Sci.* 112 (2004) 93.
- [3] Y.F. Deinega, V.M. Polyakova, L.N. Alexandrova, *Kolloidn. Zh.* 48 (1982) 546.
- [4] A. Dukhin, S. Dukhin, P. Goetz, *Langmuir* 21 (2005) 9990.
- [5] R.W. O'Brien, *J. Fluid Mech.* 190 (1988) 71.
- [6] S.B. Johnson, P.J. Scales, T.W. Healy, *Langmuir* 15 (1999) 2836.
- [7] J. Lyklema, S. Rovillard, J.D. Coninck, *Langmuir* 14 (1998) 5659.
- [8] J.B. Freund, *J. Chem. Phys.* 116 (2002) 2194.
- [9] W. Zhu, S.J. Singer, Z. Zheng, A.T. Conlisk, *Phys. Rev. E* 71 (2005).
- [10] R. Qiao, N.R. Aluru, *J. Chem. Phys.* 118 (2003) 4692.
- [11] R. Qiao, N.R. Aluru, *Phys. Rev. Lett.* 92 (2004) 198301.
- [12] R. Qiao, N.R. Aluru, *Colloids Surf. A Physicochem. Eng. Aspects* 267 (2005) 103.
- [13] R. Qiao, N.R. Aluru, *Appl. Phys. Lett.* 86 (2005) 1.
- [14] S. Joseph, N.R. Aluru, *Langmuir* 22 (2006) 9041.
- [15] L. Joly, C. Ybert, E. Trizac, L. Bocquet, *Phys. Rev. Lett.* 93 (2004) 257805.
- [16] L. Joly, C. Ybert, E. Trizac, L. Bocquet, *J. Chem. Phys.* 125 (2006) 204716.
- [17] D.M. Huang, C. Cottin-Bizonne, C. Ybert, L. Bocquet, *Phys. Rev. Lett.* 98 (2007) 177801.
- [18] D. Kim, E. Darve, *Phys. Rev. E* 73 (2006) 051203.
- [19] H.J.C. Berendsen, J.P.M. Postma, W.F. Vangunsteren, A. Dinola, J.R. Haak, *J. Chem. Phys.* 81 (1984) 3684.
- [20] D.V.D. Spoel, E. Lindahl, B. Hess, A.R.V. Buuren, E. Apol, P.J. Meulenhoff, D.P. Tieleman, A.L.T.M. Sijbers, K.A. Feenstra, R.V. Drunen, et al., *Gromacs user manual version 3.2*, 2004, URL <http://www.gromacs.org>.
- [21] J.D. Zhou, S.T. Cui, H.D. Cochran, *Mol. Phys.* 101 (2003) 1089.
- [22] T. Darden, D. York, L. Pedersen, *J. Chem. Phys.* 98 (1993) 10089.
- [23] S. Miyamoto, P.A. Kollman, *J. Comput. Chem.* 13 (1992) 952.
- [24] H.J.C. Berendsen, J.R. Grigera, T.P. Straatsma, *J. Phys. Chem.* 91 (1987) 6269.
- [25] J. Israelachvili, *Intermolecular and Surface Forces*, second ed., Elsevier Science, London, 1992.
- [26] J. Koplik, J.R. Banavar, *Annu. Rev. Fluid Mech.* 27 (1995) 257.
- [27] M. Mucha, T. Frigato, L.M. Levering, H.C. Allen, D.J. Tobias, L.X. Dang, P. Jungwirth, *J. Phys. Chem. B* 109 (2005) 7617.
- [28] H.A. Stone, A.D. Stroock, A. Ajdari, *Annu. Rev. Fluid Mech.* 36 (2004) 381, 150.
- [29] P.G. Kusalik, I.M. Svishchev, *Science* 265 (1994) 1219.
- [30] A.R. Leach, *Molecular Modeling: Principles and Applications*, second ed., Pearson, Harlow, 2001.